

Type 1 Active Galactic Nucleus Fraction in SDSS/FIRST Survey

Yu Lu, Ting-Gui Wang, Xiao-Bo Dong, Hong-Yan Zhou

¹CAS Key Laboratory for Research in Galaxies and Cosmology, University of Science and Technology of China,

²Center for Astrophysics, University of Science and Technology of China, Hefei, Anhui, 230026, P.R.China
Hefei, Anhui, 230026, China

11 November 2021

ABSTRACT

In the unification scheme, narrow lined (type 2) active galactic nuclei (AGN) are intrinsically similar to broad lined (type 1) AGN with the exception that the line of sight to the broad emission line region and accretion disk is blocked by a dusty torus. The fraction of type 1 AGN measures the average covering factor of the torus. In this paper, we explore the dependence of this fraction on nuclear properties for a sample of low redshift ($z \leq 0.35$) radio strong ($P_{1.4\text{GHz}} \geq 10^{23} \text{W Hz}^{-1}$) AGN selected by matching the spectroscopic catalog of Sloan Digital Sky Survey and the radio source catalog of Faint Image of Radio Sky at Twenty cm. After correcting for several selection effects, we find that: (1) type 1 fraction f_1 keeps at a constant of $\sim 20\%$ in the [O III] luminosity range of $40.7 < \log(L_{[\text{OIII}]})/\text{erg s}^{-1} < 43.5$. This result is significantly different from previous studies, and the difference can be explained by extinction correction and different treatment of selection effects. (2) f_1 rises with black hole mass from $\sim 20\%$ below $10^8 M_\odot$ to 30% above that. This coincides with the decrease of the fraction of highly-inclined disk galaxies with black hole mass, implying a population of Seyfert galaxies seen as Type-2 due to galaxy-scale obscuration in disk when the host galaxy type transfer from bulge-dominant to disk-dominant. (3) f_1 is independent of the Eddington ratio for its value between 0.01 and 1; (4) f_1 ascends from 15% to 30% in the radio power range of $23 < \log(P_{1.4\text{GHz}}/\text{WHz}^{-1}) < 24$, then remain a constant at $\sim 30\%$ up to 10^{26}W Hz^{-1} .

Key words: quasars: general—galaxies

1 INTRODUCTION

Active Galactic Nuclei (AGN) are traditionally divided into 2 subclasses: type 2 and type 1, according to the absence or presence of the broad emission lines. Their different observed properties can be explained largely via anisotropic obscuration, likely by a dusty torus on scales of several to tens parsecs, of otherwise the same type of objects (Antonucci 1993; Tran 1995; Nenkova et al. 2002). Because of its large physical scale, Narrow emission Line Region (NLR) cannot be (completely) obscured by such torus. Therefore, an AGN will appear as a type 2 source, when our line of sight to the Broad emission Line Region (BLR) and the accretion disk is blocked by the dusty torus. Scattered broad lines have been detected in the polarized light in almost half of type-2 AGN, which strongly supports the unification scheme (Antonucci & Miller 1985; Miller & Goodrich 1990; Moran et al. 2000).

An important parameter in this model is the opening angle of the torus. The fraction of type 1 AGN (hereafter f_1) is a measure of the average opening angle of torus in such a unification scheme. Previous studies have shown a type 2 to type 1 ratio of 3:1 for local Seyfert galaxies (e.g., Maia et al. 2003; c.f. Ho et al. 1997). How-

ever, there is no reason that the torus opening angle should be the same for every AGN, rather it may depend on the black hole mass, accretion rate, luminosity or other intrinsic parameters. Exploring these parameters dependence will be an important extension to the simple unification scheme, and yield the insight into the origin of the dust torus as well.

The luminosities of narrow emission lines, such as [O III], mid-infrared light and hard X-rays have been considered as isotropic properties (e.g. Meisenheimer et al.2001; Kauffmann et al. 2003; Wang et al. 2006). Thus, we can examine the luminosity dependence of f_1 using those luminosities. It was found that f_1 increases with [O III] luminosity in a large sample of Seyfert galaxies from Sloan Digital Sky Survey (SDSS, York et al 2000) Data Release 2 (DR2) (Simpson 2005; Hao et al. 2005). These results were interpreted in the context of “receding torus” (Lawrence 1991; Hill et al. 1996). Similar results have been reported from statistical studies of hard X-ray selected AGN (Ueda et al. 2003; Hasinger et al. 2004; Gilli et al. 2007; Hasinger et al. 2008; c.f. Wang et al. 2006).

Radio loud AGN, including radio quasars and radio galaxies, can also be unified in such scheme (see Urry & Padovani 1995 for a review). As in the case for Seyfert galaxies, broad permitted lines were detected in the polarized light of narrow line radio galaxies (e.g., Antonucci, Hurt & Kinney 1994; Tran, Cohen & Goodrich

*Email: laolu@mail.ustc.edu.cn

1995; Young et al. 1996; Tran et al. 1998). Barthel (1989) found that radio galaxies have larger linear dimensions than that of radio quasars in their 3CRR sample, and hypothesized that powerful radio galaxies and radio quasars belong to the same population, with a cone angle of $40^\circ - 50^\circ$ to mark the division between the radio quasar and galaxy. Within this scheme, by using 172 3CR radio sources, Lawrence (1991) found that the type 2 fractions are anti-correlated with radio luminosity in the range of $L_{178\text{MHz}} \geq 10^{25} \text{ W Hz}^{-1}$. Falcke et al. (1995) proposed that for radio-loud sources, jets may clear a path through the dust, and cause the obscuration along the jet's periphery, and give rise to the anti-correlation between obscuration and radio luminosity. These mentioned above only focused on the most powerful radio AGN.

In this paper, we will extend those analysis to radio moderately-strong AGN, and examine in more details f_1 as a function of radio power, [O III] luminosity, black hole mass and accretion rate using the large sample of AGN in the SDSS spectroscopic catalogues of galaxies and quasars that have been detected in Faint Image of Radio Sources at Twenty cm (FIRST, White et al. 1997). A combination of large sky coverage, high completeness to a relatively deep magnitude for galaxies and quasars, and moderate spectral resolution makes the sample ideal for such a study.

Based on the SDSS spectroscopic data set, we culled 711 type 2 objects and 286 type 1 objects having FIRST luminosity $P_{1.4\text{GHz}} \geq 10^{23} \text{ W Hz}^{-1}$ and $z \leq 0.35$. After correcting several selection effects, we obtained f_1 as a function of nuclear parameters. The paper is arranged as follows. The sample is described in the next section. The selection function is estimated in §3 and the results are presented in §4. Finally, we will discuss our result in §5. Throughout this paper, we will adopt a concordant cosmology with $H_0 = 71 \text{ km s}^{-1} \text{ Mpc}^{-1}$, $\Omega_m = 0.27$, and $\Omega_\Lambda = 0.73$ (Spergel et al. 2003).

2 THE SAMPLE OF RADIO STRONG AGN

2.1 Parent Sample

Starting with the spectroscopic samples of quasars and galaxies in the SDSS data release four (DR4), we construct the low redshift sample of radio detected galaxies and AGN. A redshift cut $z \leq 0.35$ is applied so that $H\alpha$ falls in the SDSS spectral coverage. To simplify the estimation of selection effects, we consider only the objects targeted as main galaxies (Petrosian magnitude $r \leq 17.77$ and the target mask as "TARGET_GALAXY") or low redshift quasars (psf magnitude $i \leq 19.1$ and the target mask as "TARGET_QSOs_CAP/SKIRT"), or FIRST counterparts (unresolved objects with FIRST counterparts within $2''$ and psf magnitude $i \leq 19.0$, masked as "TARGET_QSOs_FIRST_CAP/SKIRT"). This low- z galaxy and quasar sample (405,904 SDSS spectra in total) are then cross-correlated with the FIRST source catalog (Becker et al. 2003) to form the radio detected galaxy and AGN sample with a procedure described in Lu et al. (2007).

We use positional coincidence to select radio point sources, and visually inspect the FIRST images for all the candidates with extended radio morphology (refer to Lu et al. 2007 for details). Briefly, we take $2''.0$ as the cutoff of position offset for SDSS-FIRST positional coincidence, which is a trade-off between the completeness and random contamination. Then, we visually inspected the cutouts of FIRST image to select the extended lobe(s) apart from SDSS nucleus, using a degraded image of 3CR radio sources as the reference for physical association. For $z \geq 0.073$, we checked the

FIRST cutouts in $6' \times 6'$, which corresponds to a physical size of 500 kpc at the redshift $z=0.073$, because only a small number of radio sources have linear sizes larger than this. For $z \leq 0.073$, we check the cutout with an angular size corresponding to their linear sizes of 500 kpc at the sources' redshift. As the outcome of the second stage, we obtain 20,334 low redshift ($z < 0.35$) objects from SDSS-FIRST matching process.

Next, we apply a radio luminosity cutoff to the sample. According to Yun et al. (2001) and Hopkins et al. (2003), star formation (SF) galaxies rarely have radio powers larger than $P_{1.4\text{GHz}} = 10^{23} \text{ W Hz}^{-1}$. Best et al. (2005) found that the radio luminosity function at 1.4 GHz of SF galaxies intersect with radio loud AGN at $\sim 10^{23} \text{ W Hz}^{-1}$. Beyond this value, the luminosity function of SF galaxies drops dramatically, while that of radio AGN decreases mildly. Although at $\sim 10^{24} \text{ W Hz}^{-1}$, SF galaxies account for nearly 10% of the population, they will be rejected on the emission line-ratio diagrams (hereafter, BPT diagram; Baldwin, Phillips & Terlevich 1981). So we will limit our analysis to the sources with radio luminosities above $10^{23} \text{ W Hz}^{-1}$.

A k -correction to the radio luminosity is applied by assuming a radio spectral index $\alpha = 0.5$ ($f_\nu \propto \nu^{-\alpha}$). After retaining only the highest S/N spectrum for the duplicated observations, we obtain 7,810 SDSS radio loud sources, 276 from SDSS quasar sample and 7,534 from SDSS galaxy sample, at redshift $z \leq 0.35$ and with $P_{1.4\text{GHz}} \geq 10^{23} \text{ W Hz}^{-1}$.

Our criteria are similar to Best et al. (2005), who cross-correlated SDSS-FIRST "compact" sources with $3''$ and selected the "extended" radio counterparts within $30''$ by assuming that radio sources are "double lobe" or "core-lobe", but extend to a fainter limit and also include larger radio sources. These authors extracted 2,215 radio AGN and 497 SF galaxies brighter than 5 mJy (corresponding to $10^{23} \text{ W Hz}^{-1}$ at $z \sim 0.1$) from 212,000 $z < 0.3$ SDSS DR2 "main galaxies" spectroscopic targets, and their AGN classification was based on the $D_n(4000)$ versus $L_{1.4\text{GHz}}/M_*$ diagnostic plane.

2.2 Continuum Subtraction and Emission-Line Measurements

In order to classify and obtain the intrinsic properties of the radio galaxies and AGN, precise measurements of emission line fluxes are necessary. We use the measured parameters from the Value-added Extra-GALactic Catalog developed and maintained by Center for Astrophysics, University of Science and Technology of China (USTC-VEGAC; X.-B. Dong et al. in preparation). We will describe briefly the steps relevant here and leave details to the referred paper. We correct the SDSS spectra for the Galactic extinction (Schlegel, Finkbeiner & Davis 1998) using the extinction curve of Fitzpatrick (1999). The spectra are then brought into their rest frame using the redshift provided by SDSS pipeline. The continuum subtraction and emission line measurements are done separately for the different type of objects as follows:

The continuum subtraction is done according to their relative contribution of star-light and AGN continuum. For the narrow line objects, the continuum is dominated by star-light, thus, can be modeled with Independent Component templates (IC templates) following the procedures described in Lu et al. (2006).¹ In brief, we

¹ IC templates were derived from Independent Component Analysis (ICA), developed by Lu et al. (2006). Using this technique, Lu et al. (2006) compressed the synthetic galaxy spectral library to six nonnegative inde-

fit galaxy spectra with the templates derived by applying Essembling Learning for Independent Component Analysis (EL-ICA) to the simple stellar population library (Bruzual & Charlot 2003). The templates were then broadened and shifted to match the stellar velocity dispersion of the galaxy. In this way, stellar absorption lines are reasonably modeled to ensure the reliable measurement of weak emission lines. At the same time, stellar velocity dispersion, a correction to the redshift as well as an average internal extinction to the stellar light is obtained.

For nucleus dominated type 1 AGN where Fe II multiplets and other broad emission lines are highly blended, we fit simultaneously the nuclear continuum, the Fe II multiplets and emission lines (see Dong et al. 2008 for details). The nuclear continuum is approximated by a broken power-law. Fe II emission, both broad and narrow, is modeled using the Fe II templates provided by Veron-Cetty et al. (2004). For those Seyfert 1s with significant contribution of starlight as measured by the equivalent widths (EWs) of the Ca II κ λ 3934 or high order Balmer absorption lines or Na I λ 5890, 5896, a starlight model is also included using the 6 IC templates as described above. The decomposition of host-galaxy starlight, nuclear continuum and Fe II emission were carried out following the procedure as described in detail in Zhou et al. (2006).

After subtracting the continuum, we fit emission lines with multi-gaussian model using the code described in detail in Dong et al. (2005, 2008). Briefly, each line is fitted with one or more Gaussians as statistically justified (mostly with 1–2 Gaussians); the line parameters are determined by minimizing χ^2 . The [O III] λ 4959, 5007 doublet are assumed to have the same profiles and redshifts; likewise, [N II] λ 6548, 6583 and [S II] λ 6716, 6731 doublet are constrained in the same way. Furthermore, the flux ratios of [O III] doublet and [N II] doublet are fixed to the theoretical values. Usually, H α and [N II] doublets are highly blended and thus hard to be isolated; in such cases, we fit them assuming they have the same profile as [S II] doublets, which is empirically justified (e.g., Filippenko & Sargent 1988; Ho et al. 1997; Zhou et al. 2006). For the possible broad H α and H β lines, we use multiple Gaussians to fit them, as many as they could be statistically justified. If a broad emission line is detected with $S/N > 5$, we regard it as genuine. If the broad H β line is too weak to achieve a reliable fit, we then re-fit it assuming that it has the same profile and redshift as the broad H α line.

Examples of emission line modeling in H α + [N II] and H β + [O III] regions are illustrated in Figure 1. The two upper panels shown the objects which was classified by SDSS as galaxies, and the two lower ones shown the SDSS classified quasars. The total emission line flux is estimated by adding different components, while the line width is measured in the combined model.

2.3 Optical Spectral Classification

Based on the emission line parameters measured in the last section, we classify optical spectra into broad lined and narrow lined AGN, and SF galaxies, respectively. Detail criteria for each class are as follows:

Broad line AGN are culled according to the following criteria (cf. Zhang et al. 2008, X.-B. Dong et al. in preparation): (1) The broad H α component has been detected with $S/N > 5$; (2) The height of broad H α is more than twice of root mean square (RMS)

pendent components (ICs), which were proved to be good templates for modeling most normal galaxy spectra.

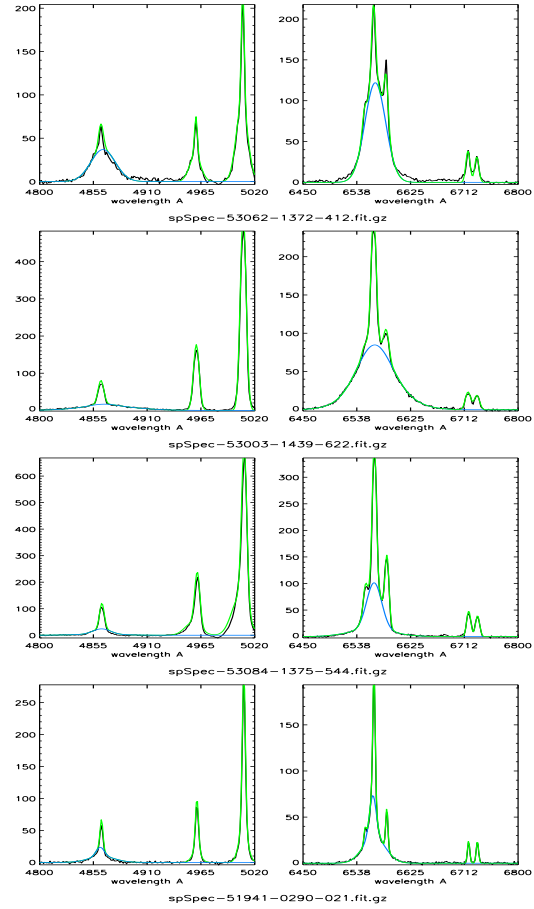


Figure 1. Emission line fitting in the H α and H β regions. The black lines represent the observed “continuum free” emission lines and noise. The blue lines represent for the fitted broad components and the green lines for broad+narrow fitting.

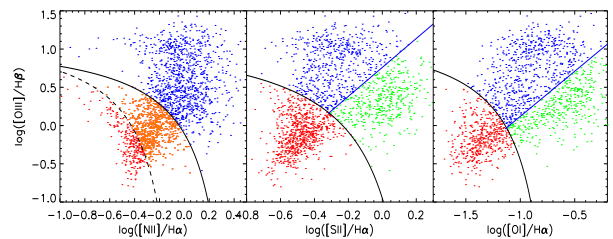


Figure 2. The BPT diagram for narrow emission line galaxies with radio luminosity $P_{1.4\text{GHz}} \geq 10^{23} \text{ W Hz}^{-1}$ and $z \leq 0.35$. The solid lines separate Seyfert from SF galaxies, and the dashed lines divide the “composite” galaxies from SF galaxies. The blue line represents for Seyfert/LINER separation.

of the continuum-subtracted spectrum in the neighbor emission-line free region to account for potential systematic errors brought in the continuum subtraction; (3) The equivalent width of broad H α line $EW(\text{H}\alpha) \geq 10\text{\AA}$, in order to eliminate potential contamination from the broad wing of the narrow component. It should be mentioned that since we use strict criteria here to select broad line AGN, we will correct the incompleteness late through simulations.

Narrow line objects are classified into SF galaxies, Seyfert 2 galaxies (Sy2), Low Ionization Nuclear Regions (LINERs) and composite galaxies, according to their locations on BPT diagrams. We adopt the empirical classification scheme proposed by Kewley

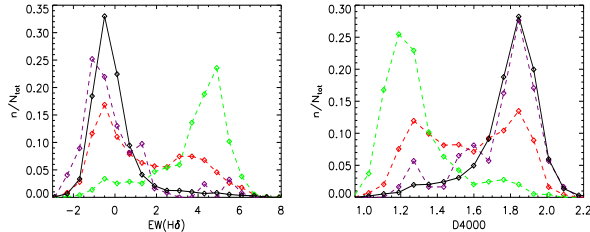


Figure 3. The distribution of H δ absorption line equivalent width (left panel) and strength of 4000Å break (right panel) for Seyfert 2 galaxies (dashed red line), SF galaxies (dashed green line), LINERs (dashed purple line), and weak lined objects (solid black line).

et al. (2006). First, we divide narrow line radio galaxies into star-forming galaxies, composite galaxies and ‘pure’ AGN on [N II]/H α versus [O III]/H β diagram. Second, ‘pure’ AGN are further separated into ‘LINER’ or Seyfert according to their locations on the [O III]/H β versus [S II]/H α or [O I]/H α diagram (see Figure 2). For 137 objects with strong detections in [O III] (with S/N > 10) but none in H β (S/N < 3), we estimate their H β by using the average H α /H β of 6.08. Most non-detections are caused by low signal to noise of the spectrum around H β region or low H β equivalent width, but not due to large extinctions. Their 3σ upper limits are consistent with the average value of H α /H β \sim 6.08.

With the above criteria, we obtain 352 broad lined objects. However, among them, 43 objects (40 galaxies, 3 quasars) do not have reliable broad H β flux (with S/N < 5), 13 ones (11 galaxies, 2 quasars) have broad line Balmer decrement (H α /H β)_{BL} > 10, in analogy with type 1.8/1.9 Seyfert galaxies (cf. Dong et al. 2005). We reject those objects from further analysis because: (1) the extinction correction to the broad or narrow lines are uncertain for objects without H β flux; (2) the sample becomes very incomplete at large Balmer decrements due to their large obscuration.

Finally, 286 broad lined objects, including 248 from SDSS quasar sample and 38 from the main galaxy sample, will be used for further analysis. We note that 55 of these Type 1 AGN (46 quasars and 9 galaxies) are Narrow-line Seyfert 1 galaxies (NLS1’s), according to the criteria of Zhou et al. (2006), with broad component of H α or H β > 10 σ confidence level and FWHM(H α) \leq 2,200 km s⁻¹. 35 of them are already included in the NLS1 sample of Zhou et al. (2006).

Among the 3,297 galaxies with detectable emission lines, 1,771 ones can be un-ambiguously classified, yielding 711 Seyfert 2 galaxies, 342 LINERs, 216 star-forming galaxies and 502 ‘composite’ galaxies. The remaining 1,526 weak emission line galaxies either do not have sufficient number of measured line ratios to allow a meaningful diagnostic on the BPT diagram (1510 objects), or the narrow line decrement H α /H β > 15 (16 objects). Most of those weak lined objects are likely to be LINERs rather than Seyfert 2 galaxies because the distributions of their H δ absorption line equivalent width and strength of 4000Å break are more similar to that of LINERs rather than Seyfert galaxies (see Figure 3). Therefore, excluding those weak lined objects will not seriously affect our estimate of type 1 fraction.

The final sample consists of 711 type 2 AGN and 286 type 1 AGN, selected from original 7810 radio galaxies and quasars with $z \leq 0.35$ and $P_{1.4\text{GHz}} \geq 10^{23}$ W Hz⁻¹. Their redshift distribution are shown in Figure 4. Their locations on the radio luminosity versus the narrow H α luminosity $L_{\text{H}\alpha}$ are shown on Figure 5. For comparison, we also add the empirical relation for SF galaxies (Yun et al.

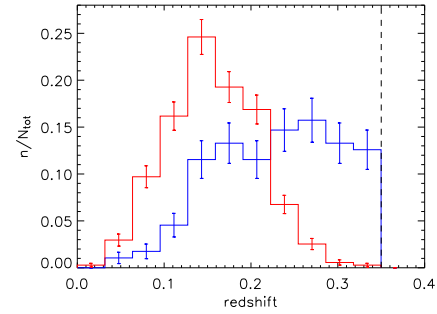


Figure 4. The redshift distribution of type 1s (blue line), and type 2s (red line).

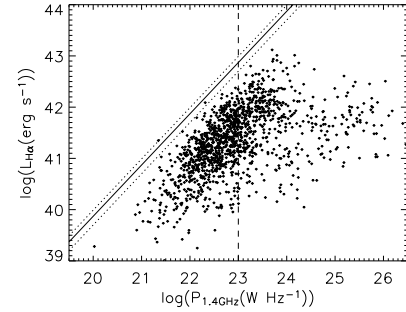


Figure 5. Radio luminosity $P_{1.4\text{GHz}}$ versus narrow H α luminosity $L_{\text{H}\alpha}$. The points represents for all SDSS selected radio AGN, regardless their radio luminosity. The solid line indicates $P_{1.4\text{GHz}} - L_{\text{H}\alpha}$ relation in SF galaxies. Beneath this line, the radio luminosity $P_{1.4\text{GHz}}$ will be barely dominated by star formation. The dashed line indicates the 10^{23} W Hz⁻¹ threshold.

2001; Kewley et al. 2002). All radio AGN locate on the lower right regime, suggesting that there is little radio contamination from the star-forming process. This is true, even if the sample is extended to a much lower radio power.

2.4 Black Hole Mass, Nuclear Luminosity and Eddington Ratio

For the Seyfert 2 galaxies, the black hole mass (M_{\bullet}) is estimated from the stellar velocity dispersion using the $M_{\bullet} - \sigma_{\ast}$ relation obtained from local host spheroids (Tremaine et al. 2002), including elliptical galaxies and the bulges of disk galaxies. The intrinsic scatter of this relation is estimated to be about 0.3 dex. The stellar velocity dispersion has been obtained by fitting the SDSS spectrum with the IC templates (refer to §2.2). It should be pointed out that the stellar light within 3’ of the SDSS fibre may contain only a fraction of galaxy spheroid or have a substantial contribution from the galactic disk. In the former case, the correction is usually small for most of our galaxies according to the formula of Jorgensen et al. (1995). In the latter case, the measured σ_{\ast} may over-estimate the stellar velocity dispersion of the bulge component in high inclination disk galaxies, or under-estimate the true value in low inclination disk galaxies. The correction depends on the size of the disk and bulge, the bulge disk ratio, the bulge velocity dispersion to the circular velocity of the disk, the distance of the galaxy, as well as the inclination of the disk. There is no simple formula for this correction. Fortunately, most radio selected AGN have large black hole masses, thus reside in the galaxies with large bulges. In these galaxies, the disk-light contamination within SDSS fibre may not be very severe. In addition, the rotational velocity is proportional to the central stellar velocity dispersion of these large galaxies (Courteau et al. 2008). Therefore, this correction may be less severe to our sample.

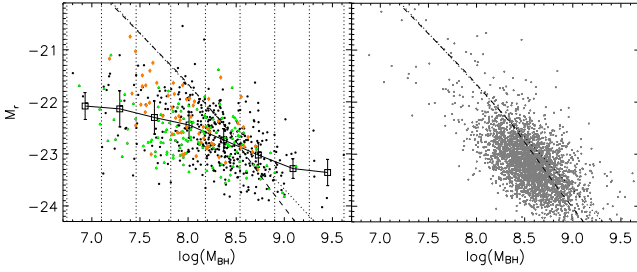


Figure 6. Black hole mass $\log(M_{\bullet})$ versus the absolute optical magnitude M_r for the radio galaxies. Left panel displays the Seyfert 2 galaxies. The orange points represent for the high inclination disk galaxies with axial ratio $b/a < 0.5$ and $\sigma_*/\text{err} > 10$, the green points for low the inclination disk galaxies with $b/a > 0.8$ and $\sigma_*/\text{err} > 10$, and black points for elliptical galaxies. The solid line shows the mean M_r value in the $\log(M_{\bullet})$ bins. The dotted line show the M_r - M_{\bullet} fitting of inactive galaxies suggested by Mclure & Dunlop (2002), and the dashed line is referred from Faber-Jackson relation of Desroches et al. (2007). The right panel displays the M_r - M_{\bullet} relation of the absorption line galaxies for comparison. The entire objects in these two panels have radio luminosity $\log(P_{1.4\text{GHz}}/\text{W Hz}^{-1}) > 23$.

In order to check whether the latter effect is important for our sample, we divide the galaxies into the disk and bulge dominated by using the profile parameters provided by SDSS pipeline. We consider it a disk galaxy if the likelihood for the exponential profile fit is larger than de Vacouleurs model fit by 0.2 dex, or inverse concentration index $\text{petroR50}/\text{petroR90} > 0.33$. Note that the concentration index criterion $C_1 = 0.33$ from Shimasaku et al. (2001) would induce a 15 ~ 20% contamination from opposite types of both disk galaxies and elliptical galaxies. But we consider this contamination acceptable. We separate the disk galaxies into high and low inclination groups according to their axial ratios (b/a ; $b/a < 0.5$ for high inclination systems, and $b/a > 0.8$ for low inclination systems). Besides, all oblate ($b/a < 0.3$) objects are considered as high inclination disks, regardless of their radial profile. Figure 6 shows their distribution on the M_r versus M_{\bullet} diagram; where M_r is the k -corrected absolute Petrosian magnitude of the host galaxy in the galaxy rest frame by interpolating the five SDSS apparent magnitudes with Spline function. For comparison, we plot the Seyfert 2 galaxies of our sample in the left panel and plot the absorption line dominated radio galaxies in the right panel. We find: (1) absorption-line dominated radio galaxies are concentrated on the high luminosity regime, while the spectroscopically type 2 AGN spread more to the lower luminosities. (2) M_r vs M_{\bullet} is tilted for type 2 AGN. It departs significantly from what is defined by the absorption line galaxies or the early type galaxies at low M_{\bullet} , and towards higher luminosity. This can be attributed most likely to the disk light contribution. (3) the high inclination galaxies (orange points) show systematically lower luminosities than that of low inclination galaxies (green points) at a given M_{\bullet} (i.e. σ_*) despite of their overlap on the plot, and they locate more closely to that of absorption line galaxies. Shao et al. (2007) showed that ‘edge-on’ galaxies are on average 0.8-0.9 fainter in magnitude than that of ‘face-on’ galaxies in the r -band due to the dust extinction. This seems sufficient to explain the offset between low inclination and high inclination disk galaxies observed here without invoking any additional effect of a disk component on the σ_* .

For type 1 AGN, the virial black hole mass can be estimated using the empirical relation between the size of BLR and continuum luminosity, and the emission line width (e.g., Wandel et al. 1999; Kaspi et al. 2005; Peterson & Bentz 2006;). We use the broad

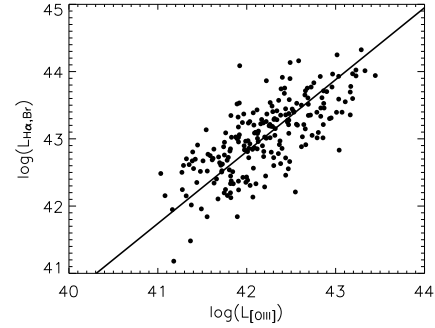


Figure 7. The [O III] luminosity $L_{[\text{OIII}]}$ versus broad $\text{H}\alpha$ luminosity $L_{\text{H}\alpha,\text{Br}}$. They are all extinction corrected on the basis of their Balmer decrement $\text{H}\alpha/\text{H}\beta$.

$\text{H}\alpha$ luminosity as a surrogate for the continuum luminosity (Wang & Zhang 2003), to account for the potential contamination from the stellar-light in the weak BLR source and from nonthermal jet emission in some cases, using the formula of Greene & Ho (2007):

$$M_{\bullet} = (3.0_{-0.5}^{+0.6}) \times 10^6 \left(\frac{L_{\text{H}\alpha}}{10^{42} \text{ergs}^{-1}} \right)^{0.45 \pm 0.03} \times \left(\frac{\text{FWHM}_{\text{H}\alpha}}{10^3 \text{kms}^{-1}} \right)^{2.06 \pm 0.06} M_{\odot}. \quad (1)$$

In section 3.3, this relation will be used also in the simulation of selection effect for the potentially overlooked broad emission lines in the observed type 2 AGN. The typical uncertainty in this relation is estimated to be around 0.5 dex (Vestergaard & Peterson 2006).

We will use reddening corrected [O III] luminosity as an indicator for the nuclear power of type 2 AGN (Mulchaey et al. 1994; Dietrich et al. 2002; Kauffmann et al. 2003; Haas et al. 2007; Netzer et al. 2006; See Reyes et al. 2008 for an extended discussion) for two reasons. First, [O III] emission is less contaminated by star-formation process, especially in these massive metal rich galaxies, than other lines such as $\text{H}\alpha$ and [O II]. Second, Balmer decrement can be used as an indicator for the global extinction to the narrow emission lines, thus the intrinsic luminosity of [O III] can be recovered based on the extinction corrected line flux.

The extinction correction to [O III] luminosity is still a complex issue. Some authors argued that the some of the Balmer lines may be totally blocked according to polarization observation (di Serego Alighieri et al. 1997). Because the ionization potential of O^+ is much higher than that of hydrogen, [O III] emission region may be even smaller than that of Balmer lines, and subject more severely to the dust extinction. Therefore, extinction derived from narrow line Balmer decrements may still underestimate the [O III] extinction. However, most of the former arguments are based on the directly observed [O III] luminosity rather than on the extinction corrected [O III] luminosity. We consider applying correction should be better than applying no correction.

We calibrate the relation between the bolometric luminosity and [O III] luminosity with the broad line radio AGN and then applied it to the type 2 objects as follows. First, we establish a relation between the extinction corrected [O III] luminosity and the broad $\text{H}\alpha$ luminosity for the type 1 radio AGN. The extinctions are estimated based on the Balmer decrements of narrow and broad lines, respectively, assuming an intrinsic $\text{H}\alpha/\text{H}\beta = 3.1$. [O III] and broad $\text{H}\alpha$ luminosities are fairly well correlated (see Figure 7).

A least-square logarithmic-linear fit yields

$$\log(L_{\text{H}\alpha,\text{Br}}) = (1.422 \pm 0.069) + (0.984 \pm 0.067) \times \log(L_{[\text{OIII}]}) \quad (2)$$

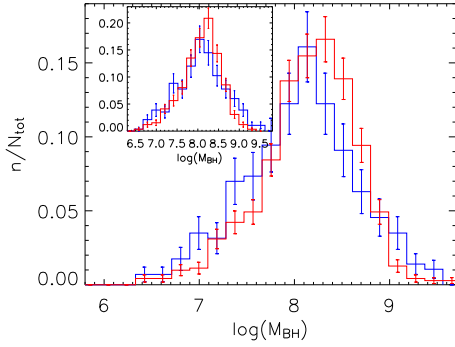


Figure 8. The black hole mass M_{\bullet} distribution of type 1s (estimated from reverberation-mapping, blue line) and that of type 2s (estimated from bulge- M_{\bullet} correlation, red line). The inset small diagram shows M_{\bullet} distribution within restricted L/L_{Edd} and L regime, refer to Figure 12 and §4.2.

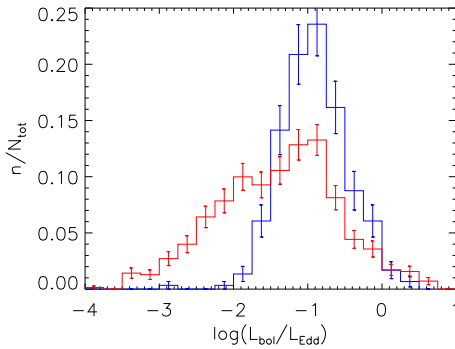


Figure 9. Eddington ratio $\log(\ell) = \log(L/L_{\text{Edd}})$ distribution for type 1s (blue line) and type 2s (red line).

, with a scatter in $\log(L_{\text{H}\alpha, \text{Br}})$ of 0.39. Note that the slope is close to one, suggesting a linear relation between the two luminosities, which is consistent with Zhang et al. (2008) for radio quiet AGN.

Second, we estimate the continuum luminosity at 5100\AA from the broad $\text{H}\alpha$ luminosity using the relation obtained by Greene & Ho (2007), for the nuclear light dominated AGN. Finally, bolometric luminosity is estimated as $L = 9(\lambda L_{\lambda})_{5100\text{\AA}}$. With the bolometric luminosity and the black hole mass, it is straight forward to calculate the Eddington ratio $\ell = L_{\text{bol}}/L_{\text{Edd}}$.

The distributions of the black hole mass for the type 1 and type 2 AGN are displayed in Figure 8. On average, the type 1 AGN have slightly smaller black hole mass than that of type 2 AGN.

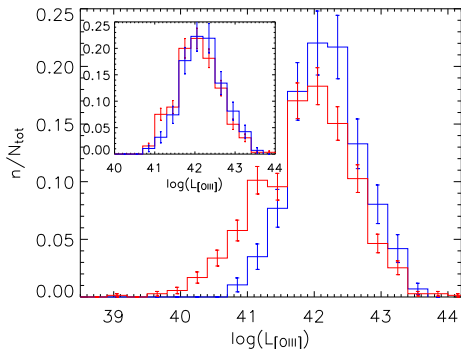


Figure 10. The extinction corrected [O III] luminosity distribution for type 1s (blue line) and type 2s (red line). The small diagram shows $L_{[\text{OIII}]}$ distribution within restricted $\log(L/L_{\text{Edd}})$ and M_{\bullet} regime, refer to Figure 12 and §4.1.

The medians are $1.0 \times 10^8 M_{\odot}$ and $1.4 \times 10^8 M_{\odot}$ for the type 1 and type 2 AGN, respectively. However, the type 1 AGN are on average 1.4 times more luminous than type 2 AGN in the extinction corrected [O III] luminosity (Figure 10). Jackson & Browne (1990) found that radio quasars are a factor 10 more luminous in the [O III] line luminosities than that of radio galaxies, and they interpreted their results as a larger extinction to narrow line region in radio galaxies than that in quasars. The difference found here is much smaller because we have corrected the intrinsic reddening using Balmer decrement while Jackson & Browne have not. Indeed, the average [O III] luminosity of the type 1 AGN is more luminous by a factor of 6 than type 2 AGN before the extinction correction. Heckman et al. (1992; see also Meisenheimer 2001) found that the mid-to far-IR emission ($\lambda \sim 6 - 50 \mu\text{m}$ in AGN rest frame) is 4 times stronger on average in quasars than that in NLRG for a 178MHz 3CR sample (including 42 quasars and 75 NLRG with $z > 0.3$). If the mid-to-far-infrared emissions are isotropic and powered by AGN, this implies that some of the NLRG may not be Seyfert 2 type but be low luminosity LINERs, or the transition of the broad line strength occurs in the low Eddington ratio and low luminosity region (see §5).

The Eddington ratio $\log(\ell) = \log(L_{\text{bol}}/L_{\text{Edd}})$ distribution was displayed in figure 9. We found that the distribution of the type 1 AGN peaked at $\log(\ell) \sim -0.9$ ($\ell \sim 0.13$) in the range of $-2 \leq \log(\ell) \leq 0$, while the distribution of the type 2 objects is wider and skewed to a lower $\log(\ell)$ although it is also peaked near $\log(\ell) \sim -0.9$. The more extended tail towards small $\log(\ell)$ in the type 2 AGN may be attributed to a selection effect because the broad line components are more difficult to be detected at a lower $\log(\ell)$. Note that scatters in the estimation of black hole mass and bolometric luminosity will cause a distortion in $\log(\ell)$ distribution. Fortunately, the scatter (0.5 dex) of the black hole estimation for type 1 using the line width and continuum luminosity is comparable to the combination of the scatter (0.3 dex) in $M_{\bullet} - \sigma_{*}$ relation and the scatter (0.4 dex) in the bolometric luminosity estimation using [O III] luminosity for type 2. Thus, the scatter effect on type 1 and type 2 distributions is similar. We will discuss this further in Section 4.

3 SELECTION EFFECTS

Selection effects are introduced during the spectroscopic target selection and the definition of narrow and broad line AGN sample. In this section we will quantify these selection effects as a function of nuclear properties for both the type 1 and type 2 AGN. We denote the number density of AGN in unit nuclear luminosity (L) and unit M_{\bullet} intervals as $\phi(L, M_{\bullet})$. The expected number of AGNs in the nuclear luminosity bin $L - L + \Delta L$ and black hole bin $M_{\bullet} - M_{\bullet} + \Delta M_{\bullet}$ can be written as,

$$\Delta N(L, M_{\bullet}) = \phi(L, M_{\bullet}) \int_{L_{\text{min}}^s(z)} p(L^s | M_{\bullet}, L) S(M_{\bullet}, L, L^s) \times dL^s V_{\text{max}}(L^s) \Delta M_{\bullet} \Delta L \quad (3)$$

where L^s is the luminosity of the band that is used in defining the magnitude limit of the sample, e.g., the r -band luminosity of the host galaxy dominated targets and i -band luminosity for the nuclear dominated targets. $p(L^s | M_{\bullet}, L)$ is the conditional probability that an AGN has L^s at the given M_{\bullet} and L . Selection function $S(M_{\bullet}, L, L^s)$ is the probability to classify the spectrum as type 1 or type 2; V_{max} is the comoving volume corresponding to the maximum redshift that an object with a luminosity L^s could be detected within the

magnitude limit. We have assumed that there is no cosmological evolution for both types of AGN within $z < 0.35$, and we will check the assumption in §3.1 and §4.1. Since we are interested in the ratio of the two type objects, and the sky coverage for type 1 and type 2 are the same, we will not consider the sky coverage for the sample in the volume calculation.

Rewriting Eq 3 for the binned data set, we find

$$\phi(L, M_\bullet) = \sum_{i=1}^N \frac{1}{V_{max,i}} \frac{h(L, L + \Delta L; M_\bullet, M_\bullet + \Delta M_\bullet)}{\int_{L_{lim}^s}^{\infty} p(L^s | M_\bullet, L) S(M_\bullet, L, L^s) dL^s} \quad (4)$$

for N AGN in the sample, and $h(L, L + \Delta L; M_\bullet, M_\bullet + \Delta M_\bullet)$ is the rectangular function. Due to the additive nature of Eq 4, AGN selected via exclusive rules can be added up simply.

With $\phi(L, M_\bullet)$, we can obtain the density of AGN in the unit interval of Eddington ratio $\ell = L_{bol}/L_{Edd}$ and M_\bullet :

$$\varphi(\ell, M_\bullet) = \int \phi(L, M_\bullet) \delta(\ell - \ell(L)) (\partial \ell(L) / \partial L)_{M_\bullet} dL \quad (5)$$

The density at radio luminosity bin could be wrote as

$$\psi(P_{1.4\text{GHz}}) = \int \phi(L, M_\bullet) p(P_{1.4\text{GHz}} | L, M_\bullet) dL dM_\bullet \quad (6)$$

, where $p(P_{1.4\text{GHz}} | L, M_\bullet)$ is the conditional probability that an AGN has a radio luminosity of $P_{1.4\text{GHz}}$ at a given M_\bullet and L .

3.1 V_{max}

Different magnitude limits have been used in the selection of different type spectroscopic targets. The apparent magnitude limits for main quasars and FIRST counterparts are $i_{psf} \leq 19.1$ on the psf magnitude, while for galaxies it is $r_{\text{Petrosian}} \leq 17.77$ in r band. We calculate V_{max}^{opt} for each object according to its relevant optical magnitude limit and the corresponding optical luminosity². Since our objects were detected by FIRST, which has a detection limit of $f_{1.4\text{GHz}} \geq 1\text{mJy}$, a V_{max}^{radio} can be estimated from the radio power and the radio flux limit for each object. Furthermore, we adopt a cutoff in the redshift $z \leq 0.35$, so the maximum volume is $V_{0.35}$. The V_{max} is the smallest one among the above three values.

For objects uniformly distributed in the universe, the average $< V/V_{max} >$ will be around 0.5. We calculated this value for both type 1 and type 2 AGN. We find $< V/V_{max} > = 0.55$ for the type 1 AGN, and $< V/V_{max} > = 0.54$ for the type 2 AGN. This may be taken as an evidence that the number density of AGN increases mildly with increase redshift, and we will discuss the evolution effect in §4.1.

3.2 The Probability Function for Type 2s

Ignoring the contribution of emission lines to the optical magnitude, the type 2 AGNs are selected according to their host galaxies. In order to quantify the conditional probability $p(L^s | M_\bullet, L)$ of type 2 AGN for a given black hole mass and nuclear luminosity (or [O III] luminosity), we need to establish a relation among the host galaxy magnitude L^s , the [O III] luminosity $L_{[\text{OIII}]}$, and the black hole mass M_\bullet . The strong correlation between the mass of the massive black hole and the bulge luminosity of its host

² Because we are interested in the ratio of type 1 and type 2 AGNs, rather than their comoving density, we do not take the survey area into consideration.

galaxy was established for the bulge dominated quiescent galaxies in the local universe (e.g., Häring & Rix 2004) and for the active galaxies and quasars (e.g., Peng et al. 2006). However, there is still controversial whether this relation depends on the level of nuclear activity (McLure & Dunlop 2002). To check this, we divide the type 2 AGN into high ($\log(L_{[\text{OIII}]}/\text{erg s}^{-1}) > 42$) and low ($\log(L_{[\text{OIII}]}/\text{erg s}^{-1}) < 42$) [O III] luminosity groups, and examine their distributions on $M_r - M_\bullet$ diagram. We find that at the same M_\bullet , the [O III] luminous galaxies are brighter than the low $L_{[\text{OIII}]}$ counterparts for only 0.1-0.2 mag on average, which can be accounted for by their different emission line luminosities. Therefore, we will assume that the host's luminosity is independence of the nuclear luminosity at a given black hole mass. Therefore, we write $p(L^s | M_\bullet, L)$ as $p(L^s | M_\bullet)$, i.e., independence of the nuclear luminosity L .

The galaxies are selected based on their Petrosian magnitudes, i.e., L^s should be the total magnitude of the galaxy. In order to quantify $p(L^s | M_\bullet)$, we need to characterize the relation between the black hole mass and the total luminosity of its host galaxy, and the scatter of this relation as well. For the known Seyfert 2 galaxies, their distributions are already shown in Figure 6. We assume the including of the missed Seyfert galaxies does not change this relation. Because the disk contribution increases as the black hole mass decreases, the relation between the galaxy luminosity and black hole mass is flatter than the bulge-black hole relation shown in Figure 6. For comparison, we also show the $M_\bullet - M(\text{bulge})$ relation for the inactive galaxies: $\log(M_\bullet) = -0.50(\pm 0.05)M_R(\text{bulge}) - 2.91(\pm 1.04)$ (McLure & Dunlop 2002), and the Faber-Jackson relation of Desroches et al. (2007) for the normal elliptical galaxies. Apparently, $M_r - \log(M_\bullet)$ relation of our sample is much flatter than the latter relations. To describe quantitatively the distribution of the M_r as a function of M_\bullet , we calculate the average value and the second momentum of M_r over each M_\bullet bin, and approximately estimate the $p(L^s | M_\bullet)$ with a gaussian distribution around their mean value.

We assume the type 2 galaxies are relative easy to identify, so $S(M_\bullet, L, L^s) = 1$ once the object is observed spectroscopically. This assumption will fail in two cases: (1) nuclear emission lines are too weak, so that some lines used in the spectral classification cannot be detected in the spectrum with a typical signal to noise ratio of the main galaxy sample; (2) the contamination of the emission lines from the HII regions of its host galaxy makes the spectral classification as composite or HII type. In the first case, we will miss very weak type 2 AGN, i.e., the low Eddington ratio objects. But this will not affect our study of the type 1 to type 2 ratios, because the detection of a type 1 AGN will require an even higher Eddington ratio, and our analysis is limited to the parameter space that a substantial fraction of both the type 1 and type 2 can be detected (see Figure 12). In the second case, we will drop some of the type 2 AGN in the late type of galaxies, which tend to have lower black hole masses. We will discuss this in §4.2.

3.3 The Selection Function for Type 1s

The probability of identifying a type 1 object depends on the signal to noise ratio of the spectrum and broad line parameters, its profile and intensity, in a rather complicated manner. To quantify such a selection effect, we generate a large number of spectra covering the $H\alpha$ blending and $H\beta$ regimes using Monte-Carlo simulations similar to what has been done by Hao et al. (2005) but taking additional parameters, like the intrinsic reddening and black hole mass, into consideration. These spectra are modeled in exactly the same

way as we did for the real data to obtain the emission line parameters, and the type 1 objects are selected with the same criteria as described in §2.3. This will give the probability of selecting a type 1 AGN under different physical parameter regime.

A simulated emission line spectrum is the sum of three components: the narrow line spectrum (f_{narrow}), broad line spectrum (f_{broad}) and the noise spectrum (noise). In order to mimic the diverse narrow line spectrum and to avoid complicated noise model, we use the observed narrow line spectrum and noise spectrum. In order to explore the physical parameters as broad as possible, we take the narrow line plus noise spectrum from both the type 1 and type 2 AGN.

The narrow line plus the noise spectrum ($f_{\text{narrow}} + \text{noise}$) is obtained by subtracting the power-law continuum and FeII models for the nuclei dominated objects, or by subtracting the stellar continuum model for the host galaxy dominated objects from the observed spectrum. It should be noted that this treatment of noise spectrum is in-exact for the Seyfert 2 galaxies, because the addition of a broad line component and its corresponding nuclear continuum would also increase the noise. But its effect is likely to be small because a broad line with a height of ten percent of the continuum flux would be easily detectable in most spectra.

For the broad line spectrum (f_{broad}), we estimated them with the parameters of line profile and line flux, which in turn depends on the intrinsic broad-line luminosity and the dust extinction to the BLR. We denotes the broad line component as,

$$f_{\text{broad}} = A(\lambda)Kf_{\text{broad}}^s \quad (7)$$

where $A(\lambda)$ and K are the internal extinction and the scaling factor, respectively, and f_{broad}^s is 'standard' broad line spectrum.

For the type 1 objects, f_{broad}^s is the best fitted model for both broad H β and H α after correcting for the internal reddening. For the Seyfert 2 objects, we assume that the broad line profile can be approximated with a single gaussian, and the line width can be estimated from the empirical relation in Eq.1, with the black hole mass estimated from $M - \sigma_*$ relation, and line-flux obtained from the observed [O III] luminosity with Eq.2.

$A(\lambda)$ comes from a set of eight extinction values, which corresponds to a uniformly distributed H α /H β values between 3-10, assuming the intrinsic H α /H β =3.1. For a given $A(\lambda)$, a set of ten K_n are created randomly following the H α luminosity distribution at the observed [O III] luminosity, i.e., $p(L_{\text{H}\alpha}|L_{\text{[OIII]}})$ (see Figure 7).

To summarize, for each AGN, we build a set of simulated spectra that has identical narrow line+noise spectrum as the observed spectrum but with a series of manually-built broad line components. Assuming the nuclei luminosity scaled with broad line, the apparent magnitude and volume limit will change when we vary f_{broad} component of Seyfert galaxies. We retained only those K_n and $A(\lambda)$ that makes the optical flux for the simulated spectrum within the magnitude limit ($r < 17.77$ for the host dominated objects and $i < 19.1$ for the nuclear dominated objects). As a result, up to 80 spectra are created for each observed AGN.

We measure the emission line parameters of these simulated spectra and determine whether they are broad line AGN as for the real spectra. In this way, for each object, we obtain a probability as a function of the black hole mass, un-attenuated nuclear luminosity, the amount of extinction, and apparent magnitude, i.e., $S(M_*, L, E_{B-V}, L^s)$. With this selection function, we can estimate approximately the distribution of E_{B-V} from the observed one by assuming that the real E_{B-V} distribution does not depend on the black hole mass and optical luminosity. Under this assumption, we can correct the observed E_{B-V} distribution using the above simu-

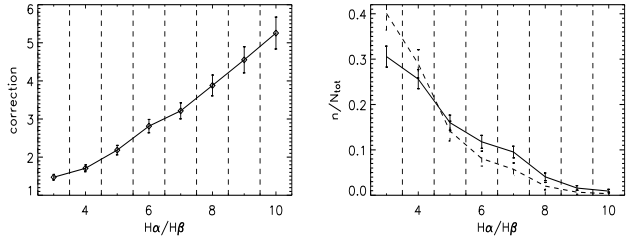


Figure 11. Left panel: average correction factor $N^{\text{id}}(E_{B-V})/N^{\text{sim}}(E_{B-V})$ along Balmer decrement $(\text{H}\alpha/\text{H}\beta)_{\text{BL}}$. Right panel: the observed (dashed line) and corrected (solid line) Balmer decrement distribution.

lated spectrum

$$p(E_{B-V}) = p^{\text{obs}}(E_{B-V})N^{\text{id}}(E_{B-V})/N^{\text{sim}}(E_{B-V}). \quad (8)$$

where the $p^{\text{obs}}(E_{B-V})$ and $p(E_{B-V})$ are the observed and real distribution of E_{B-V} ; $N^{\text{id}}(E_{B-V})$ and $N^{\text{sim}}(E_{B-V})$ are the number of spectra identified as Seyfert 1 galaxies and total number of the simulated spectra that meet the SDSS targeting criteria. For this correction, we have assumed that E_{B-V} distribution is independent of black hole mass and nuclear luminosity. The assumption has not been fully tested, however, it should not dramatically affect our result as far as the correction remains small or the dependence is weak. The observed and corrected H α /H β is displayed in Figure 11. In comparison with the observed one, which peaks at 3.1, and is identical to the value reported by Dong et al. (2008), the corrected H α /H β distribution shows much more objects at higher extinctions. Integrating over the distribution of E_{B-V} , we yield:

$$S(M_*, L, L^s) = \int S(M_*, L, E_{B-V}, L^s)p(E_{B-V})dE_{(B-V)} \quad (9)$$

Because the correction increases fast with the degree of extinction, one must keep in mind that the true number may become less reliable at higher extinctions. For this reason, we will limit our analysis only to $E_{B-V} < 1.3$ (i.e., H α /H β < 10), the same criteria we adopted in the type 1 AGN selection.

For quasars, the conditional probability $p(L^s|M_*, L) = \delta(L^s - L)$ and $S(M_*, L, L^s)$ is independent of L^s . For the broad line objects selected from the galaxy sample, there is a distribution of L^s for a given nuclear luminosity and black hole mass due to the significant contribution from the host galaxy. Using the relation between the host galaxy and the black hole for the type 2 Seyfert galaxies (see Figure 6) and the nuclear luminosity from $L_{\text{H}\alpha, \text{Br}} - L_{5100}$ relation (refer to Greene & Ho 2007), we write

$$p(L^s|M_*, L) = \frac{1}{2\pi\sigma_1\sigma_2} \int dL^{\text{host}} \exp\left(-\frac{(L^{\text{host}} - L^{\text{host}}(M_*))^2}{2\sigma_1^2}\right) \times \exp\left(-\frac{(L^s - L^{\text{host}} - L_r(L))^2}{2\sigma_2^2}\right) \quad (10)$$

where $L^{\text{host}}(M_*)$ is the average r -band host luminosity in the AGN rest frame for a black hole mass M_* , and σ_1 is the scatter of this relation; $L_r(L)$ is the average r -band nuclear luminosity for a given L which is estimated via the broad H α luminosity. As we already seen, σ_2 is much smaller than σ_1 , so we can approximate the second part of the integrand as a δ function.

We show contours of the average selection function on the black hole mass versus nuclear luminosity plane in Figure 12. The selection function strongly depends on the BH mass and nuclear luminosity [O III]: the incompleteness increases towards larger black

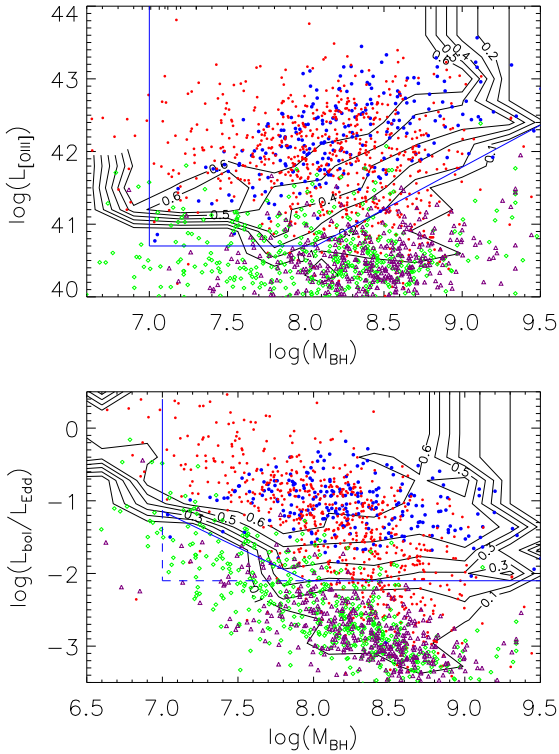


Figure 12. The contour of selection function and the restricted regime of $\log(M_*/M_\odot) > 6.6$, $\log(L_{[\text{OIII}]}/\text{erg s}^{-1}) > 40.7$ and $\log(L_{\text{bol}}/L_{\text{Edd}}) > -2.1$ (blue lines). The red circles represent for type 2s, blue circles for type 1s, purple triangles for LINERs, and green diamonds for composite galaxies. The contour levels were set from 0.1 to 0.6, with interval of 0.1.

hole mass and lower luminosities. At $[\text{O III}]$ luminosity below $10^{40.7}$ erg s^{-1} , the selection function is below 0.2, even at black hole mass as low as $10^8 M_\odot$. The dearth of type 1 AGN below this limit can be well attributed to the selection effects.

4 THE TYPE 1 FRACTION

With all the above corrections, we will analyze the fraction of the type 1 AGN as a function of the basic parameters, such as black hole mass, accretion rate, nuclear luminosity and radio power. As we can see in the Figure 12, due to selection effect, the type 1 AGN can be detected to a reasonable fraction only in a very limited parameter space on either M_* versus $\log(L/L_{\text{Edd}})$ plane or $L_{[\text{OIII}]}$ versus M_* plane. In order to avoid potentially large uncertainties introduced with our correction of selection effects, we will limit our analysis to the parameter regimes of $\log(M_*/M_\odot) > 6.6$, $\log(L_{[\text{OIII}]}/\text{erg s}^{-1}) > 40.7$ and $\log(L_{\text{bol}}/L_{\text{Edd}}) > -2.1$, that a substantial fraction of Type 1 AGN are detected. Using the selection function $S(M_*, L, L^s)$, V_{max} and $p(L^s|M_*, L)$ in the last section, we can calculate $\phi(M_*, L)$ for broad and narrow line AGN.

4.1 The Dependence of Type 1 Fraction on $L_{[\text{OIII}]}$

The regime of M_* and $L_{[\text{OIII}]}$ used in this analysis is illustrated in the upper panel of Figure 12 with blue lines. In this regime, $\log(L_{[\text{OIII}]})$ distribution of type 1s and type 2s are very similar with means $\log(L_{[\text{OIII}]}/\text{erg s}^{-1})$ of 42.47 and 42.40 for type 1 and type 2 AGN, respectively (see inserted small diagram in Figure 10). We integrate $\phi(M_*, L_{[\text{OIII}]})$ over either M_* in the corresponding range to get

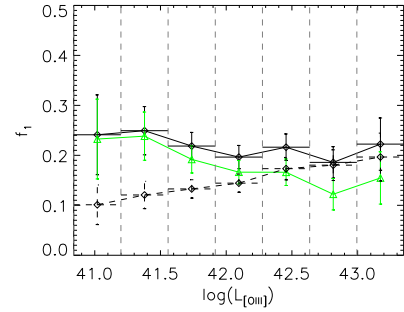


Figure 13. The dependence of type 1 fraction on $L_{[\text{OIII}]}$ for observed density (dashed line and diamonds), bias corrected density (solid line and diamonds), and maximum redshift evolution corrected density (green line and triangles). The evolution correction is based on extrapolation of quasar luminosity function of Richards et al. (2005).

$\phi(L_{[\text{OIII}]})$ for both type 1 and type 2 AGN. It is straight forward to calculate the type 1 fraction by dividing the bias-corrected type 1 objects density by the total AGN density in each bin. The results are show in Figure 13.

The observed type 1 fraction increases with $L_{[\text{OIII}]}$, which is similar to, but with a flatter slope than those given by Simpson (2005, hereafter S05) and Hao et al. (2005, hereafter H05) for radio quiet AGN. After correcting for selection effects, f_1 keeps at nearly a constant value of 20% over the $[\text{O III}]$ luminosity range $40.7 < \log(L_{[\text{OIII}]}/\text{erg s}^{-1}) < 43.5$. The least χ^2 fit for a constant f_1 yields $f_1 \sim 20.1\%$ which is acceptable at a probability of 0.92. This result is different from S05 and H05, who found that the fraction of Type 1 AGN increases significantly with the nuclear luminosity for mainly radio quiet AGN. The difference can not be considered (solely) as a difference between radio-loud and radio quiet AGN, but be attributed to several different treatments. First, S05 and H05 does not corrected $[\text{O III}]$ luminosity for the internal extinction, while such a correction is included in this work. It is known that type 2 Seyfert galaxies show systematically larger Balmer decrements of narrow lines than Type 1 Seyfert galaxies (Cohen 1983; Gaskell 1984; Rhee & Larkin 2005). This extinction would reduce the $[\text{O III}]$ luminosities of Seyfert 2 galaxies with respect to the Seyfert 1 galaxies systematically. In fact, before extinction correction, the type 1 fraction in our sample would also increase dramatically from $\sim 10\%$ at $\log(L_{[\text{OIII}]}/\text{erg s}^{-1}) \sim 41$ to $\sim 90\%$ at $\log(L_{[\text{OIII}]}/\text{erg s}^{-1}) \sim 43$. Second, Type 2 AGN in the S05 includes also LINERs and composite type AGN. While it is still controversy whether composite type 2 AGN are of similar nature as Seyfert galaxies, those spectroscopic LINERs are certainly different from Seyfert galaxies (Kauffmann et al. 2003; Kewley et al. 2006; Heckmann et al. 2004). Also we note that most composite galaxies are located in relative lower black hole mass and LINERs on lower accretion rate regime, while broad lined AGN seldom fall in these regions (refer to Figure 12). Third, as seen in Figure 12, the difference can be attributed at least partly to that we focus our analysis to the limited parameter regime. Outside the regime, type 2 AGN are detected in large amount but almost no type 1 object has been detected on the regime with large black hole mass and small $[\text{O III}]$ luminosity. Finally, S05 did not consider selection effect at all while H05 used a different selection function. However, as seen in the Figure 12, this changes the $[\text{O III}]$ luminosity dependence only moderate. This is understandable because we limit our analysis to the parameter regime, where the correction is only modest.

Hitherto we ignored the redshift evolution, but V/V_{max} test does show mild positive evolution with z . We estimate the maximal impact of the evolution on our result by using the double power-law

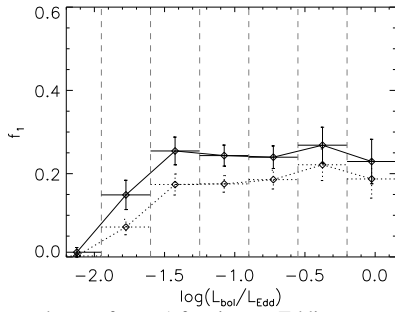


Figure 14. The dependence of type 1 fraction on Eddington ratio $\log(\ell) = \log(L/L_{\text{Edd}})$ for observed density (dashed line) and bias corrected density (solid line).

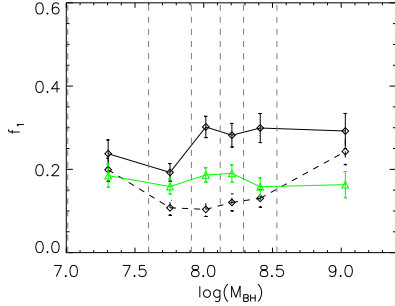


Figure 15. The dependence of type 1 fraction on M_{\bullet} for the bias corrected density (f_1^{cor} , solid black line and diamonds), the observed density (f_1^{obs} , dashed black line and diamonds), and simulated type 1 density (f_1^{sim} , green line and triangles, based on the convolved type 2 density). Each bin contains the same number of sources.

form quasar luminosity function $\Phi(L, z)$ for $z < 2.1$ derived from 2dF-SDSS LRG and quasar survey (Richards et al. 2005). Assuming that type 1s and type 2s evolved in the same form, in every $\{L, z\}$ bin, we can apply correction of $\Phi(L, z = 0)/\Phi(L, z)$ to both type 1s and type 2s. The result is shown in figure 13 (green line and triangles). The redshift evolution pulls down the type 1 fraction by ~ 6 percent at high luminosity end, but change little at low luminosity end. As expected, this effect does not significantly alter our result.

4.2 The Dependence of Type 1 Fraction on M_{\bullet} and Eddington ratio

The regimes of M_{\bullet} and $\ell = L_{\text{bol}}/L_{\text{Edd}}$ used in this analysis are shown in the bottom panel of Figure 12. In this regime, the average M_{\bullet} for type 1s ($\sim 10^{8.04} M_{\odot}$) and type 2s ($\sim 10^{8.11} M_{\odot}$) are indistinguishable (see small diagram in Figure 8). Within the regime, we integrate $\phi(L, M_{\bullet})$ over either L in the corresponding range to get $\phi(M_{\bullet})$. Similarly, by integrating of $\varphi(M_{\bullet}, \ell)$ (see Eq.5) over M_{\bullet} , we can obtain $\varphi(\ell)$ for both type 1 and type 2 AGN. Note that our analysis is restricted to the parameter range illustrated in Figure 12 (blue lines), where a substantial fraction of both type 1 and type 2 AGN are detected. Thus we can calculate the type 1 fraction straightly by dividing the bias-corrected type 1s density by the total AGN density in each $\log(\ell)$ bin and $\log(M_{\bullet})$ bin. The results are show in Figure 14 and Figure 15.

From Figure 14, we find that the type 1 fraction keeps nearly a constant value of 25% when Eddington ratio changes from $\log(\ell) \simeq -1.5$ to $\log(\ell) \simeq 0.0$ for the black hole mass in the range of $6.6 < \log(M_{\bullet}/M_{\odot}) < 9.5$. We also note that the correction to selection effects is only modest in whole range of Eddington ratio, and does not significantly affect our conclusion as shown in the Figure 12. In fact, before the correction for selection effects, type 1 fraction is more consistent with a constant value over $-1.5 < \log(\ell) < 0.0$.

At lower Eddington ratios, type 1 fraction becomes very low, and the transition occurs at $\log(\ell) \sim -2$. The transition is likely real, rather than caused by under-estimate of the selection function. As seen in Figure 12, most detected objects in this region are massive objects, and the value of the selection function is between 0.3 and 0.5. Lack broad emission line of those objects maybe represent a true difference in the BLR properties or over-luminous of [O III] in comparison with its true nuclear luminosity in this parameter region.

As mentioned in §2.4, the uncertainty in the black hole estimate will broaden the distribution, thus affect our results about the dependence of type 1 fraction on black hole mass. Black hole masses for type 2 are estimated using the $M_{\bullet} - \sigma_{*}$ relation. This relation has an intrinsic scatter of only 0.3 dex, while the Type 1 BH masses are estimated using the Virial estimator, which may affected by the inclination of the AGN and accretion rate, and has a typical uncertainty of a factor of 0.5 dex. Because this larger scatter, a tail to high masses and low mass would be greater for the Type 1s than the Type 2s when cut-off (such as $L_{[\text{OIII}]}$) is applied. When a ratio of Type 1 over Type 2 is taken, this would then give an increasing Type-1 fraction at high and low black hole masses as observed.

In order to correct this bias, we convolve the type 2 $\log(M_{\bullet})$ distribution with a Gaussian of $\sigma = 0.4$, so that type 1s and type 2s have the same scatter. We restrict to objects in $\{L_{[\text{OIII}]}, M_{\bullet}\}$ region, as shown in upper panel of Figure 12. Based on convolved type 2 density $\rho_{\text{type2}}^{\text{conv}}$, the simulated type 1 density fraction $f_1^{\text{sim}} = \rho_{\text{type1}}^{\text{obs}} / (\rho_{\text{type1}}^{\text{obs}} + \rho_{\text{type2}}^{\text{conv}})$ was displayed in Figure 15, represented with green line and triangles. While the observed type 1 density fraction $f_1^{\text{obs}} = \rho_{\text{type1}}^{\text{obs}} / (\rho_{\text{type1}}^{\text{obs}} + \rho_{\text{type2}}^{\text{obs}})$ was represented with dashed line and diamonds. Therefore, in every $\log(M_{\bullet})$ bin, we could correct the selection effect from different M_{\bullet} measurement uncertainty for a factor of $f_1^{\text{sim}}/f_1^{\text{obs}}$. Combining it with selection function and detection probability, we plot the type 1 fraction $f_1^{\text{cor}} = \phi_1 / (\phi_1 + \phi_2)$ dependence on $\log(M_{\bullet})$ in figure 15 with solid line. The least χ^2 fit for a constant f_1 yields $\chi^2 = 15.54$ for 5 degrees of freedom, which rules out a constant f_1 at a confidence level of $\sim 99\%$. From the figure, we can see that the type 1 fraction is $\sim 30\%$ in higher BH mass region ($\log(M_{\bullet}/M_{\odot}) > 8$), about 10 percent higher than that in lower M_{\bullet} region. f_1 also rises in the BH mass bin below $\log(M_{\bullet}/M_{\odot}) < 7.6$. This may be due to the loss of type 2 AGN in this sample. Low mass black holes are usually hosted in the disk galaxies with relative small bulge, such galaxies are more likely to have a star forming disk. Due to relative large aperture of SDSS fibre, SDSS spectrum will encompass also the star forming disk. This will shift some type 2 Seyfert galaxies into the composite-type. Because we consider only Seyfert 2 type spectra, those type 2 AGN will be missed in our Seyfert 2 sample (refer to the ‘‘composite galaxies’’ in Figure 12, represented with green points). In order to check the fraction of such objects, we examine the distribution on the BPT diagram of type 1 AGN, which are selected based solely on the presence of broad lines. We find that only 4.05% (9) type 1s with $\log(M_{\bullet}/M_{\odot}) > 7.6$ show composite spectra on BPT diagram, while 21.3% (16) of broad line AGN with $\log(M_{\bullet}/M_{\odot}) < 7.6$ do. This confirms our suspicion that the contamination of star-formation region becomes more important at low black hole masses.

4.3 The Dependence of Type 1 Fraction on Radio Properties

We plotted the distribution of radio luminosity $P_{1.4\text{GHz}}$ in the left panel of Figure 16. It is clear that more type 2 AGN distribute near the lower $P_{1.4\text{GHz}}$ limit $10^{23} \text{ W Hz}^{-1}$ than type 1 objects, and fewer

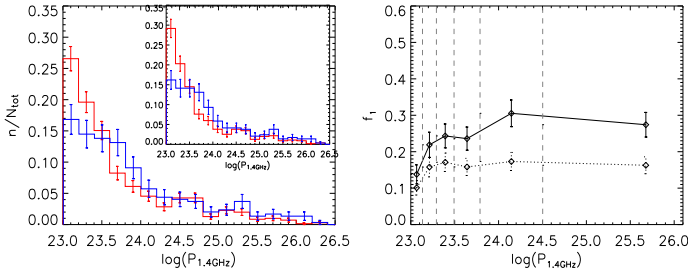


Figure 16. Left panel: the radio power $P_{1.4\text{GHz}}$ distribution for type 1s (blue line) and type 2s (red line). The small diagram shows $P_{1.4\text{GHz}}$ distribution within restricted $\log(L/L_{\text{Edd}})$ and $\log(M_{\bullet})$ regime, refer to Figure 12. Right panel: the dependence of type 1 fraction on $P_{1.4\text{GHz}}$ for observed density (dashed line) and bias corrected density (solid line). Each bin in right panel contains the same number of sources.

type 2 objects in the high radio luminosity region $P_{1.4\text{GHz}} > 10^{25}$ W Hz^{-1} . After limiting to radio AGN in the parameter regime defined in Figure 12, the overall distribution is also quite similar. The type 1 fraction increases from 15% at $\log(P_{1.4\text{GHz}}/\text{W Hz}^{-1}) = 23$ to nearly 30% at $\log(P_{1.4\text{GHz}}/\text{W Hz}^{-1}) = 24$ and then flattened to $\log(P_{1.4\text{GHz}}/\text{W Hz}^{-1}) = 26$ (Figure 16). Note that the trend is very similar before and after correction for selection effects. χ^2 -test rules out the possibility of a constant f_1 at a confidence level of 99.5%. However, when the lowest radio power bin is removed, the trend in the rest 5 bins is consistent with a constant f_1 at a probability of 50%. Lawrence et al. (1991) found that type 2 fraction decreases with radio power for a lower frequency selected 3CR radio sample, which consists of mainly powerful radio sources. Since our sample includes only a smaller number of powerful ($P_{1.4\text{GHz}} > 10^{26}$ W Hz^{-1}) radio sources, this is not adequate to address whether f_1 rises at high radio luminosity.

Comparing to lower frequency selected samples, our sample is more likely affected by radio selection effects. It is general considered that radio emission from an AGN consists of two components, an isotropic extended lobe component and a beamed jet component (e.g., Urry & Padovani 1995). When the AGN is viewed along the radio jet, the jet component with a relative flat radio spectrum is boosted relativistically, while the lobe emission with a steep spectrum remains the same, i.e., high frequency radio flux is boosted along the jet direction more than low frequency radio flux. As such, a high frequency survey is more sensitive to the core-dominated or compact, flat-spectrum sources than to the lobe-dominated or diffused, steep-spectrum sources. Because it is general believed that the jet emerges along the symmetric axis, the sample will be biased to the face-on system, whose optical spectrum is type 1 in unified scheme.

The beaming effect can be checked with radio morphology. A radio AGN will appear as a double-lobe source when it is observed side-away, and as core-jet or core dominated structure viewed along the jet direction due to beaming effect of the relativistic jet. Therefore, the core dominance parameter, defined as $C = P_c/P_t$ ($P_t = P_c + P_l$), as a rough indicator of the system inclination. If radio jet aligns with the symmetric axis of the dusty torus, one would expect that type 1 fraction increases with C . However, only about 12% sources in our sample have resolved radio structures. The number is still too small to allow to reach a firm conclusion on this.

5 SUMMARY AND DISCUSSION

We have quantified several selection effects on the AGN classification and spectral targeting for different combinations of host galaxy properties, nuclear properties and dust extinction from spectroscopic samples of radio loud SDSS galaxies and quasars using Monte-Carlo simulations. Type 1 AGN have much strong selection effect than type 2 AGN. Type 1 radio AGN can be studied only in a very limited parameter space on the black hole mass versus Eddington ratio or luminosity diagram. After correction for these selection effects, we find that in the limited parameter region: (1) type 1 fraction is nearly independent of extinction-corrected $[\text{O III}]$ luminosity and Eddington ratio at $\log(L_{[\text{O III}]}/\text{erg s}^{-1}) > 40.7$ and $\log(\ell) > -1.5$; at very low Eddington ratio, there are almost no type 1 AGN, which can not be accounted for solely by selection effects, indicating a transition in the broad line strength around $\log(\ell) \sim -2$ (see also Hopkins et al. 2009). (2) The type 1 fraction increases with the radio power from 10^{23} to 10^{24} W Hz^{-1} , then keep flat until 10^{26} W Hz^{-1} . (3) The type 1 fraction is $\sim 30\%$ in $M_{\bullet} > 10^8 M_{\odot}$ region, $\sim 10\%$ higher than that in lower M_{\bullet} region.

Our result on the luminosity dependence is quite different from previous studies for radio loud quasar and galaxies (Lawrence 1991; Hill et al. 1996; Reyes et al. 2008), or mainly radio quiet AGN from SDSS (Simpson 2005, Hao et al. 2005). The difference can be mainly attributed to three factors. First, we use an extinction corrected $[\text{O III}]$ luminosity while previous authors did NOT. The average Balmer decrements of narrow components for Seyfert 2 galaxies (~ 6.08) is significantly higher than for Seyfert 1 galaxies (~ 3.59), which will give rise to a factor of 5 difference in $[\text{O III}]$ luminosity for two type of Seyfert galaxies. Second, we restricted our analysis to the parameter regimes, where a substantial fraction of objects can be detected according to selection function, this reduces the uncertainty caused by the correction of selection effects. The final parameter regime used here is similar to the one that found by Hopkins et al. (2009) based on a different approach. This cuts down the objects with very low Eddington ratios and high black hole mass, thus raises the type 1 fraction in the low luminosity end. Finally, our AGN classification is based on more recent work of Kewley et al. (2006), which gives a better separation of LINERs and Seyfert galaxies. The new criteria removes quite some more LINERs than the previous criteria. Because most of these LINERs have lower $[\text{O III}]$ luminosity (see Figure 12), this raises significantly the fraction of type 1 in the low luminosity.

Although the X-ray observed AGN sample do not suffer from above selection effects, however, the fraction of type 1 object based on the optical classification into broad and narrow lined objects suffers from the aforementioned selection effects. Thus it is probably the same reasons caused a luminosity-dependence of obscured type-1 (Hasinger et al. 2008; Gilli et al. 2007; Fiore et al. 2008). Rowan-Robinson et al. (2009) using infrared to X-ray spectral energy distribution as a classification for obscured and un-obscured AGN, and they reached a similar conclusion as this paper.

Two very different phenomenological models have been proposed for the unification of broad and narrow line radio AGN. The receding torus model was first proposed by Lawrence (1991) to explain the decrease of the fraction of narrow line objects with the optical luminosity in radio loud AGN, and was extended to radio quiet objects later (Hill et al. 1996; Simpson 2005; Hao et al. 2005; Suganuma et al. 2006). The basic idea is that the opening angle of the dust torus is larger for more luminous AGN because dust sublimation radius increases with nuclear luminosity while the height of the torus is assumed to be independent of the bolometric luminosity.

Thus the broad-line region can be seen over a larger opening angle in more luminous objects. On the other hand, Grimes et al. (2004) showed that observations are consistent with dual population radio sources, 'starved' low luminosity AGN, which do not have a broad emission line region, and 'Eddington-tuned' high luminosity AGN, without invoking a receding model. In our analysis, we excluded these very low Eddington ratio objects³. Our results show that the torus opening angle does not change with the nuclear luminosity, thus do not support 'receding torus' model, but are consistent with the two population models.

Very little has been known about the dependence of the type 1 fraction on black hole mass or accretion rate. Using the ratio of infrared to bolometric luminosity as an indicator of subtending angle of torus, Cao (2005) found that the opening angle of torus increases with the central black hole for a sample of Palomer-Green quasars, but does not correlate with its Eddington ratio. On the other hand, Zhou & Wang (2005) argued that the subtending angle of torus decreases with increasing accretion rate based on the equivalent width of narrow FeK α line. It should be noted that the origin of the narrow FeK α is not clear and the equivalent width is also sensitive to the column density of the absorbing material. Our results agree with Cao et al. (2005) in the region of $\log(M_{\bullet}/M_{\odot}) > 7.6$.

It is difficult to compare our results with theoretical models of dusty torus. Most dynamic-based dusty torus models are not able to predict quantitatively how the opening angle of torus changes with the black hole mass or Eddington ratio, although some relation may be expected. In the dusty cloud model, the physical process that maintains a thick torus is still not clear (Krolik & Begelman 1988; Zier & Biermann 2002). Beckert & Duschl (2004) proposed that a geometrically thick torus can be sustained at a high accretion rate by the balance of energy dissipation due to cloud-cloud collision and heating due to accretion. They found a torus height to radius ratio $H/R \sim \sqrt{2GM/(c_s \dot{M}(R))}$, where \dot{M} is the accretion rate, $M(R)$ the mass within radius R , and c_s sound speed. Their model has a clear prediction that subtending angle of the torus increases with the accretion rate. Our results do not support this. Radiation pressure support is suggested by Pier & Krolik (1992), and the infrared radiation and local heating pressure can be very effective in supporting a smooth distributed torus. However, an equilibrium solution can be found only in a relative narrow Eddington ratio range (Krolik 2007; Shi & Krolik 2008). It has still to be demonstrated that models taken into consideration of more physical processes, such as instability, would finally lead to a prediction of a constant torus opening angle over a fairly broad Eddington ratios.

In an alternative model of disk outflow, the entrained dusty cold clouds are responsible for the obscuration (e.g., Konigl & Kartje 1994). Dopita et al. (1998) suggested that the torus and the accretion disk may interact by accretion-outflow feedback process. Elitzur & Shlosman (2006) argued that a torus is present only at nuclear luminosity greater than 10^{42} erg s⁻¹, and its covering factor decreases with increase luminosity. However, its argument is based on a strong assumption that the size of dusty clouds are scaled only with their launching radius. On the other hand, numerical simulations showed that luminous and high accretion rate ($L_{\text{bol}}/L_{\text{Edd}}$) AGN are likely strongly affected by obscuration in the disk wind models (Schurch, Done & Proga 2009).

It should be noted that there are obscuration sources other than dusty torus. The large-scale galactic dust lane and the nuclear star-

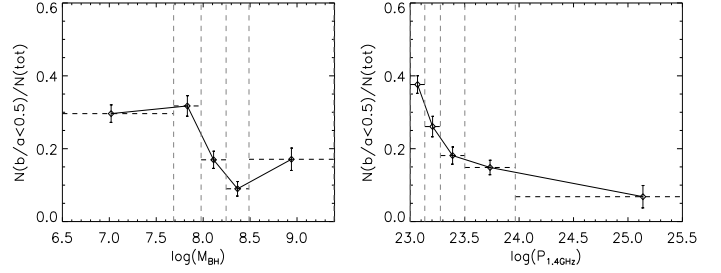


Figure 17. The fraction of high inclination ($(b/a)_{\text{exp}} < 0.5$) type 2s among disk host galaxies. Left panel displayed its dependence on $\log(M_{\bullet})$, and the right panel displayed its dependence on $\log(P_{1.4\text{GHz}})$. Each bin contains the same number of sources.

burst region are certainly responsible for obscuration in some of observed type-2 AGN. As we have noticed that a fraction of type-2 objects in the sample resides in relative edge-on disk galaxies. In Fig 17, we displayed the fraction of high inclination ($b/a < 0.5$) type 2 galaxies among disk host galaxies. The fraction decreases quickly as black hole mass and radio luminosity increases. This matches almost exactly the variations in f_1 with M_{\bullet} found in Fig 15: a $\sim 10\%$ step function in M_{\bullet} at around $10^8 M_{\odot}$. Also, the decrease of the edge-on disks fraction in right panel of Fig 17 may be related to the large increase of f_1 in the lowest radio power bin in Fig 16. These results can be explained by the presence of a population of Seyfert galaxies, seen as Type-2 due to galaxy-scale obscuration. Therefore, the increase of type 1 fraction with black hole mass and radio luminosity may be understood as that host galaxies moves gradually from disk to early-type galaxies, the extinction by the host galaxy decreases. This result offer a very different interpretation from the rest of the paper discusses.

6 ACKNOWLEDGEMENT

We thank the anonymous referee for useful suggestions to improve the paper. This work was supported by the Chinese NSF through NSF-10973013 and 973 program 2007CB815403. This paper has made use of the data from the SDSS and FIRST. Funding for the creation and distribution of the SDSS Archive has been provided by the Alfred P. Sloan Foundation, the Participating Institutions, the National Aeronautics and Space Administration, the National Science Foundation, the US Department of Energy, the Japanese Monbukagakusho and the Max Planck Society. FIRST is funded by the National Astronomy Observatory (NRAO), and is a research facility of the US National Science foundation and uses the NRAO Very Large Array.

REFERENCES

- Antonucci, R. R. J., & Miller, J. S. 1985, *ApJ*, 297, 621
- Antonucci, R. 1993, *ARA&A*, 31, 473
- Antonucci, R., Hurt, T., & Kinney, A. 1994, *Nature*, 371, 313
- Baldwin, J. A., Phillips, M. M., & Terlevich, R. 1981, *PASP*, 93, 5
- Barthel, P. D. 1989, *ApJ*, 336, 606
- Becker, R. H., Helfand, D. J., White, R. L., Gregg, M. D., & Laurent-Muehleisen, S. A. 2003, *VizieR Online Data Catalog*, 8071, 0
- Beckert, T., & Duschl, W. J. 2004, *A&A*, 426, 445

³ Most of low Eddington ratio objects (with $L/L_{\text{Edd}} < 0.01$) are LINERs (see Figure 12).

- Best, P. N., Kauffmann, G., Heckman, T. M., & Ivezić, Ž. 2005, *MNRAS*, 362, 9
- Bruzual, G., & Charlot, S. 2003, *MNRAS*, 344, 1000
- Cao, X. 2005, *ApJ*, 619, 86
- Cohen, R. D. 1983, *ApJ*, 273, 489
- Courteau, S., McDonald, M., & Widrow, L. M. 2008, IAU Symposium, 245, 227
- Desroches, L.-B., Quataert, E., Ma, C.-P., & West, A. A. 2007, *MNRAS*, 377, 402
- Dietrich, M., Hamann, F., Shields, J. C., Constantin, A., Vestergaard, M., Chaffee, F., Foltz, C. B., & Junkkarinen, V. T. 2002, *ApJ*, 581, 912
- Dong, X.-B., Zhou, H.-Y., Wang, T.-G., Wang, J.-X., Li, C., & Zhou, Y.-Y. 2005, *ApJ*, 620, 629
- Dong, X., Wang, T., Wang, J., Yuan, W., Zhou, H., Dai, H., & Zhang, K. 2008, *MNRAS*, 383, 581
- Dopita, M. A., Heisler, C., Lumsden, S., & Bailey, J. 1998, *ApJ*, 498, 570
- Elitzur, M., & Shlosman, I. 2006, *ApJ*, 648, L101
- Falcke, H., Gopal-Krishna, & Biermann, P. L. 1995, *A&A*, 298, 395
- Filippenko, A. V., & Sargent, W. L. W. 1988, *ApJ*, 324, 134
- Fiore, F., et al. 2008, *ApJ*, 672, 94
- Fitzpatrick, E. L. 1999, *PASP*, 111, 63
- Gaskell, C. M. 1984, *Astrophys. Lett.*, 24, 43
- Gilli, R., Comastri, A., & Hasinger, G. 2007, *A&A*, 463, 79
- Greene, J. E., & Ho, L. C. 2007, *ApJ*, 670, 92
- Grimes, J. A., Rawlings, S., & Willott, C. J. 2004, *MNRAS*, 349, 503
- Haas, M., Siebenmorgen, R., Pantin, E., Horst, H., Smette, A., Käuffl, H.-U., Lagage, P.-O., & Chini, R. 2007, *A&A*, 473, 369
- Hao, L., et al. 2005, *AJ*, 129, 1795
- Häring, N., & Rix, H.-W. 2004, *ApJ*, 604, L89
- Hasinger, G. 2004, Nuclear Physics B Proceedings Supplements, 132, 86
- Hasinger, G. 2008, *A&A*, 490, 905
- Heckman, T. M., Chambers, K. C., & Postman, M. 1992, *ApJ*, 391, 39
- Heckman, T. M., Kauffmann, G., Brinchmann, J., Charlot, S., Tremonti, C., & White, S. D. M. 2004, *ApJ*, 613, 109
- Hill, G. J., Goodrich, R. W., & Depoy, D. L. 1996, *ApJ*, 462, 163
- Ho, L. C., Filippenko, A. V., Sargent, W. L. W., & Peng, C. Y. 1997, *ApJS*, 112, 391
- Hopkins, A. M., et al. 2003, *ApJ*, 599, 971
- Hopkins, P. F., Hickox, R., Quataert, E., & Hernquist, L. 2009, arXiv:0901.2936
- Jackson, C. A., & Browne, I. W. 1990, *Nature*, 343, 43
- Jorgensen, I., Franx, M., & Kjaergaard, P. 1995, *MNRAS*, 276, 1341
- Kaspi, S., Maoz, D., Netzer, H., Peterson, B. M., Vestergaard, M., & Jannuzi, B. T. 2005, *ApJ*, 629, 61
- Kauffmann, G., et al. 2003, *MNRAS*, 346, 1055
- Kewley, L. J., Geller, M. J., Jansen, R. A., & Dopita, M. A. 2002, *AJ*, 124, 3135
- Kewley, L. J., Groves, B., Kauffmann, G., & Heckman, T. 2006, *MNRAS*, 372, 961
- Konigl, A., & Kartje, J. F. 1994, *ApJ*, 434, 446
- Krolik, J. H., & Begelman, M. C. 1988, *ApJ*, 329, 702
- Krolik, J. H. 2007, *ApJ*, 661, 52
- Lawrence, A. 1991, *MNRAS*, 252, 586
- Le Borgne, J.-F., et al. 2003, *A&A*, 402, 433
- Lu, H., Zhou, H., Wang, J., Wang, T., Dong, X., Zhuang, Z., & Li, C. 2006, *AJ*, 131, 790
- Lu, Y., Wang, T., Zhou, H., & Wu, J. 2007, *AJ*, 133, 1615
- Maia, M. A. G., Machado, R. S., & Willmer, C. N. A. 2003, *AJ*, 126, 1750
- McLure, R. J., & Dunlop, J. S. 2002, *MNRAS*, 331, 795
- Meisenheimer, K., Haas, M., Müller, S. A. H., Chini, R., Klaas, U., & Lemke, D. 2001, *A&A*, 372, 719
- Miller, J. S., & Goodrich, R. W. 1990, *ApJ*, 355, 456
- Moran, E. C., Barth, A. J., Kay, L. E., & Filippenko, A. V. 2000, *ApJ*, 540, L73
- Mulchaey, J. S., Koratkar, A., Ward, M. J., Wilson, A. S., Whittle, M., Antonucci, R. R. J., Kinney, A. L., & Hurt, T. 1994, *ApJ*, 436, 586
- Nenkova, M., Ivezić, Ž., & Elitzur, M. 2002, *ApJ*, 570, L9
- Netzer, H., Mainieri, V., Rosati, P., & Trakhtenbrot, B. 2006, *A&A*, 453, 525
- Peng, C. Y., Impey, C. D., Ho, L. C., Barton, E. J., & Rix, H.-W. 2006, *ApJ*, 640, 114
- Peterson, B. M., & Bentz, M. C. 2006, *New Astronomy Review*, 50, 796
- Pier, E. A., & Krolik, J. H. 1992, *ApJ*, 399, L23
- Reyes, R., et al. 2008, *AJ*, 136, 2373
- Rhee J. H., Larkin J. E., 2005, *ApJ*, 620, 151
- Richards, G. T., et al. 2005, *MNRAS*, 360, 839
- Rowan-Robinson, M., Valtchanov, I., & Nandra, K. 2009, *MNRAS*, 941
- Schlegel, D. J., Finkbeiner, D. P., & Davis, M. 1998, *ApJ*, 500, 525
- Schurch, N. J., Done, C., & Proga, D. 2009, *ApJ*, 694, 1
- Shao, Z., Xiao, Q., Shen, S., Mo, H. J., Xia, X., & Deng, Z. 2007, *ApJ*, 659, 1159
- Shi, J., & Krolik, J. H. 2008, *ApJ*, 679, 1018
- Simpson, C. 2005, *MNRAS*, 360, 565
- Spergel, D. N., et al. 2003, *ApJS*, 148, 175
- Suganuma, M., et al. 2006, *ApJ*, 639, 46
- Tran, H. D. 1995, *ApJ*, 440, 597
- Tran, H. D., Cohen, M. H., & Goodrich, R. W. 1995, *AJ*, 110, 2597
- Tran, H. D., Cohen, M. H., Ogle, P. M., Goodrich, R. W., & di Serego Alighieri, S. 1998, *ApJ*, 500, 660
- Tremaine, S., et al. 2002, *ApJ*, 574, 740
- Ueda, Y., Akiyama, M., Ohta, K., & Miyaji, T. 2003, *ApJ*, 598, 886
- Urry, C. M., & Padovani, P. 1995, *PASP*, 107, 803
- Véron-Cetty, M.-P., Joly, M., & Véron, P. 2004, *A&A*, 417, 515
- Vestergaard, M., & Peterson, B. M. 2006, *ApJ*, 641, 689
- Wandel, A., Peterson, B. M., & Malkan, M. A. 1999, *ApJ*, 526, 579
- Wang, T.-G., & Zhang, X.-G. 2003, *MNRAS*, 340, 793
- Wang, J. X., & Jiang, P. 2006, *ApJ*, 646, L103
- White, R. L., Becker, R. H., Helfand, D. J., & Gregg, M. D. 1997, *ApJ*, 475, 479
- York, D. G., et al. 2000, *AJ*, 120, 1579
- Young, S., Hough, J. H., Efstathiou, A., Wills, B. J., Bailey, J. A., Ward, M. J., & Axon, D. J. 1996, *MNRAS*, 281, 1206
- Yun, M. S., Reddy, N. A., & Condon, J. J. 2001, *ApJ*, 554, 803
- Zhang, K., Wang, T., Dong, X., & Lu, H. 2008, *ApJ*, 685, L109
- Zhou, X.-L., & Wang, J.-M. 2005, *ApJ*, 618, L83
- Zhou, H., Wang, T., Yuan, W., Lu, H., Dong, X., Wang, J., & Lu, Y. 2006, *ApJS*, 166, 128
- Zier, C., & Biermann, P. L. 2002, *A&A*, 396, 91